Journal of Solid State Chemistry **155,** 206–215 (2000)
doi:10.1006/jssc.2000.8935, available online at http://www.idealibrary.com on IDEAL®

High-Temperature Incommensurate-to-Commensurate Phase Transition in the Bi_2MoO_6 Catalyst

D. J. Buttrey,*[,1] T. Vogt,† and B. D. White*

*Center for Catalytic Science and Technology, Department of Chemical Engineering, University of Delaware, Newark, Delaware 19716; and †Physics Department, Brookhaven National Lab, Upton, New York 11973

Received June 8, 2000; in revised form August 9, 2000; accepted August 15, 2000

DEDICATED TO PROFESSOR J. M. HONIG

The temperature-dependent behavior of the low- and intermediate-temperature phases of γ-Bi_2MoO_6 were investigated. As revealed by high-resolution neutron and synchrotron powder diffraction as well as electron diffraction, the low-temperature Aurivillius phase shows a previously undetected incommensurate modulation along the pseudo-tetragonal a ($q_a = 0.5626(2)$) and c ($q_c = 0.2844(2)$) axes. A reversible incommensurate-to-commensurate phase transition to the intermediate-temperature phase occurs near 840 K, before irreversibly transforming near 880 K into the fluorite-related high-temperature polymorph described in detail by two of us in an earlier study (Buttrey *et al.*, *J. Solid State Chem.* 111, 118–127 (1994)). © 2000 Academic Press

INTRODUCTION

Despite the importance of complex oxides in catalysis, our understanding of the interplay between crystal structure and catalytic properties is far from well developed. Bismuth molybdates are prototypical bimetallic oxide catalysts contained in multicomponent molybdate (MCM) preparations that are widely used for the selective oxidation and ammoxidation of olefins (1). The oxidation of propylene to acrolein, for instance, is achieved with a selectivity of up to 95%. The two steps involved in the process are hydrogen abstraction at a bismuth site, resulting in an allyl intermediate, followed by an oxygen insertion at an adjacent molybdenum site to generate the product. The conversion of 1-butene to 1,3-butadiene is also effectively accomplished with these materials. With the addition of ammonia, the ammoxidation of propylene to produce acrylonitrile provides another very important application of the bismuth molybdates. Beyond the requirement of site isolation (2) in the topological arrangement of the bismuth and molybdenum reaction sites, which can be accomplished with the appropriate structural motifs, factors such as the surface area and crystal habit, surface reconstruction, site potentials, and stability to oxidation and reduction cycling are important. Note that these are redox catalysts, involving simultaneous reduction and reoxidation to avoid net loss of lattice oxygen.

The three catalytically active bismuth molybdates have rather similar Bi:Mo ratios. These ratios are 2:3 (α-$Bi_2Mo_3O_{12}$), 1:1 (β-$Bi_2Mo_2O_9$), and 2:1 (γ-Bi_2MoO_6). The α phase is often described as a defective scheelite structure in which 1 of every 3 Bi sites is vacant (3). For our purposes, it is useful to recognize that the scheelite structure is a special case of the fluorite family. The β form is again a fluorite-related superstructure with metal site vacancies; one of every nine metal sites is absent. In both cases, the vacancies are in an ordered arrangement (at room temperature) within infinite Bi channels (5). The γ composition shows polymorphism. The low-temperature polymorph, a (rare) naturally occurring mineral called koechlinite, is generally thought to be the catalytically active form since this is the stable bulk phase under reaction conditions (i.e., $\sim$ 650–750 K). Interestingly, the highest temperature form is the only one of 3 γ polymorphs that is clearly a fluorite derivative with infinite Bi channels, though unlike α and β, it has no vacant metal sites. The low and intermediate γ forms both belong to the Aurivillius family (6), $(Bi_2O_2)_x$ $(Bi_{n-1}MO_{3n+1})$, with $x, n = 1$ and M = Mo (7). These consist of a strongly distorted nearly square layered network of Mo polyhedra separated by $\{Bi_2O_2\}^{2+}$ layers. These Mo polyhedra are usually described as distorted octahedra, in contrast to the isolated tetrahedra evident in the fluorite-type bismuth molybdates. As we will show, they are actually somewhat intermediate between octahedra and tetrahedra.

The γ-Bi_2MoO_6 composition has been the subject of considerable attention and controversy due to its three-phase polymorphism (8). When heated from room temperature, it first undergoes a subtle and reversible phase transition near 840 K involving a poorly understood change between the closely related $n = 1$ Aurivillius-type structures

[1]To whom correspondence should be addressed.

0022-4596/00 $35.00

discussed above. We will designate the lowest temperature polymorph as γ(L) and the next lowest (intermediate as γ(I), consistent with the convention of Kodama and Watanabe (9). With further heating, the transition to the high-temperature form, designated here as γ(H), involves an irreversible first-order transition at 877 K to a fluorite-related phase (9, 10). Interestingly, this high-temperature polymorph is very closely related to the α and β structures in that all possess fluorite-related substructures, yet catalytic proficiency is attributed to the α, β, and γ(L) forms. The structure of the γ(H) phase was refined earlier from high-resolution neutron powder diffraction data (10). Note that an alternative convention sometimes used to indicate the low-, intermediate-, and high-temperature phases, which we will not follow here, is γ, γ'', and γ'. Our attention in this paper will be on the thermal evolution of the γ(L) and γ(I) forms. These are the only reported (fully oxidized) bismuth molybdates that are not obvious fluorite-derived structures, although it should be recognized that the Bi_2O_2 layers within these structures are locally fluorite-like. In this comparison, we include the more bismuth-rich phases $Bi_{26}Mo_{10}O_{69}$ (11, 12) and $Bi_{38}Mo_7O_{78}$ (13), as other fluorite-type examples.

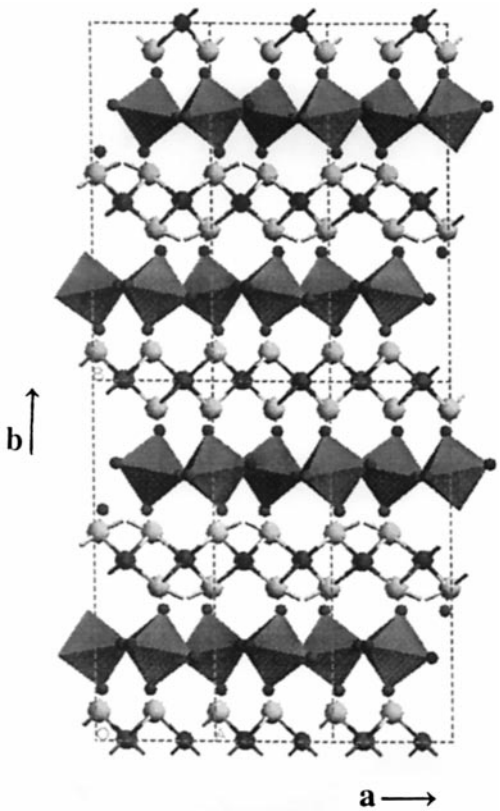

FIG. 1. The structure of γ(L)-Bi_2MoO_6 viewed down the **c** axis. The MoO_6 octahedra share corners along **a** and **c**, forming infinite $\{MoO_4\}$ layers that alternate with $\{Bi_2O_2\}$ layers along **b**. The stacking sequence along **b** is $\{Bi[2]_2O[2]_2\}$–O[1]–$\{MoO[4]_{2/2}O[5]_{2/2}\}$–O[6]–$\{Bi[1]_2O[3]_2\}$–O[6]–$\{MoO[4]_{2/2}O[5]_{2/2}\}$–O[1]–.

In γ(L)-Bi_2MoO_6, alternating layers of $\{Bi_2O_2\}^{2+}$ and $\{MoO_4\}^{2-}$ layers are stacked perpendicular to the **b** axis (Fig. 1). In the $\{Bi_2O_2\}^{2+}$ layer, the Bi^{3+} ion has a pyramidal coordination to O[2] and O[3] and a sterochemically active lone pair. There are two distinguishable $\{Bi_2O_2\}^{2+}$ layers in the structure: one $\{Bi[2]_2O[2]_2\}^{2+}$ layer being connected along **b** to the adjacent $\{MoO_4\}^{2-}$ layers by oxygen O[1] and the other $\{Bi[1]_2O[3]_2\}^{2+}$ layer connecting via O[6] to the neighboring $\{MoO_4\}^{2-}$ layers. The molybdenum has highly distorted octahedral coordination with four equatorial oxygen sites involving pairs of O[4] and O[5] and two apical oxygens (O[1] and O[6]). The MoO_6 octahedra share corners along **a** and **c** to form an infinite $\{MoO_4\}_n$ layer. The stacking sequence along **b** is thus

$$\cdots\text{–}\{Bi[2]_2O[2]_2\}\text{–}\{O[1]\text{–}MoO[4]_{2/2}O[5]_{2/2}\text{–}O[6]\}\text{–}$$

$$\{Bi[1]_2O[3]_2\}\text{–}\{O[6]\text{–}MoO[4]_{2/23}O[5]_{2/2}\text{–}O[1]\}\text{–}\cdots.$$

This structure is somewhat similar to the K_2NiF_4 structure, but with an extra layer of oxygen in the midplane of the rock salt layer. Ignoring distortions, the ideal structure would be tetragonal with space group $Im4/mm$ (a nonstandard setting of $I4/mmm$ ($\#139$)), and with all $\{Bi_2O_2\}^{2+}$ layers equivalent. The deviations from this parent structure are due to distortions within the two metal–oxygen layers. Octahedrally coordinated Mo(VI), being a d^0 transition metal, is subject to a second-order Jahn–Teller distortion, leading to the displacement of the cation from the center of the octahedron (14). This lowers the energy of the vacant d orbitals for the small and highly charged Mo(VI) cation. If lowered sufficiently, they will interact with the filled oxygen p orbitals. In extended structures the near degeneracy of molecular orbitals close to the Fermi level will usually give rise to an instability that will be removed by structural distortions. Molybdenum(VI) is known to show very strong valence distortions since it satisfies the two necessary conditions for the above scenario: (i) a small energy gap between the highest occupied (HOMO) and lowest unoccupied molecular orbital (LUMO) and (ii) a distortion mode of the same symmetry as the HOMO-to-LUMO transition.

In γ(L)-Bi_2MoO_6 the apical oxygens are shifted in opposite directions along **a**, leading to tilted corner-sharing octahedral chains along **a**. The molybdenum atom itself is not at the center of the octahedron, but displaced toward one of the O[4]–O[5] edges, leading to two shorter and two longer equatorial distances. This produces a symmetry closer to tetrahedral C_{2v} rather than C_{3v} or C_{4v}. Note that, in γ(H)-Bi_2MoO_6, all Mo sites are present as isolated, slightly distorted tetrahedra, hence close to C_{2v} also.

The oxygen atoms in the $\{Bi_2O_2\}^{2+}$ layers are also laterally shifted in the **a** direction. The different Bi–O distances in the $\{Bi_2O_2\}^{2+}$ layer can be understood as

rationalized by Albright *et al.* (15): Electron transfer from the perovskite layer via the lone pair of O[1] and/or O[6] to the antibonding σ^* in either of the Bi_2O_2 layers will weaken the bonding to the two oxygens in the *trans* position. This is due to the so-called "*trans* effect". One oxygen that is twice subject to the *trans* effect is expected to have the longest Bi–O distance and one that is not affected by any charge transfer will reveal the shortest Bi–O distance.

EXPERIMENTAL

Synthesis and Preliminary Characterization

A 15-g polycrystalline sample of γ(L)-Bi_2MoO_6 was prepared from a stoichiometric mixture of 99.9% Bi_2O_3 and 99.95% MoO_3. The mixture was heated in a covered alumina crucible in air with the following sequence: 500°C for 48 h with an interruption at 24 h for regrinding, 580°C for 6 days, and after regrinding and pressing into a pellet, another 8 days at 580°C. The intensely yellow product (as compared with pale yellow for the quenched high-temperature polymorph) was determined to be phase pure to within the detection limits by conventional X-ray powder diffraction using a Philips PW1710 system with a Cu$K\alpha$ source and a graphite monochromator on the detector arm. A second harmonic generation (SHG) measurement was positive (16), confirming that the structure is noncentrosymmetric, consistent with the space group $Pca2_1$ reported by Theobald *et al.* (17).

High-Resolution Neutron Powder Diffraction

The neutron powder diffraction data were collected on the high-resolution neutron powder diffractometer (HRNPD) on beamline H1A at the High Flux Beam Reactor at Brookhaven National Laboratory (BNL). The instrument was equipped with a new type of monochromator made of a 30-cm-tall vertically focusing array of 24 Ge (115) composites positioned at a take-off angle of 120°, providing a wavelength of 1.8857 Å. Further details on the monochromator are described elsewhere (18, 19). The resolution of $\Delta d/d \sim 5 \times 10^{-4}$ was achieved using 5′ primary collimation in front of the monochromator and 5′ collimators in front of each of the 64 ^{3}He detectors. The 15-g specimen was contained in a vanadium can and mounted on a closed-cycle displex refrigerator for a measurement at 20 K (determined using a Si diode). High-temperature data were collected with calibrated Type-K thermocouples placed on the top and bottom of the specimen. The data were refined using the Rietveld refinement (20) program PROFIL written by Cockcroft and Fitch (21).

Electron Diffraction

For the TEM studies, grain mounts onto holey carbon films were prepared and mounted in a double-tilt holder. The electron microscope used was a Philips CM-400T operating at 100 keV.

Synchrotron X-Ray Powder Diffraction

Synchrotron X-ray powder data were collected on the X7A beamline at the BNL National Synchrotron Light Source. The specimen was mounted on a flat plate for room temperature study. A channel cut Si(111) crystal was used for the double monochromator on the incident side and a Ge(220) crystal analyzer was present on the detector arm.

DISCUSSION

Room Temperature Studies

Rietveld refinements. The symmetry of γ(L)-Bi_2MoO_6 at room temperature was a subject of controversy until Theobald *et al.* (17) showed that the appropriate space group was noncentrosymmetric $Pca2_1$ using high-resolution neutron powder diffraction. This is consistent with the structure originally proposed by van den Elzen and Rieckh (7), the ferroelectric behavior reported by Ismailzade *et al.* (22), and the SHG measurement on our specimen mentioned earlier. We have not ruled out the possibility of a symmetry change below the γ(L)/γ(I) transition, although we were unable to find any space group (centrosymmetric or noncentrosymmetric) that would better represent the data.

Analyzing data taken at room temperature, we noted slight deviations between the observed and calculated intensities and profiles that could not be explained by strain and/or particle size effects. A close examination revealed that very small satellites with about 0.1% of the intensity of the strongest Bragg reflection and could not be attributed to the starting reagents or any other obvious potential contaminant (Fig. 2a). This prompted us to investigate our sample using electron diffraction.

Transmission electron microscopy. Numerous selected area electron diffraction patterns were obtained for the [010] zone. Many of these patterns show weak superstructures, all revealing streaking along **a*** and/or **c***. Three representative patterns, each of which was observed more than once, are shown in Figs. 3a–3c. In Fig. 3a the pattern only shows streaking with no evidence for any further superstructure. Figure 3b depicts a pattern in which the satellites appear with displacements of approximately $(\pm n/4, 0, 0)$ about the principle Bragg reflections, and which are superimposed on the streak. The first harmonic is by far the most intense, and in most patterns this is the only one apparent in the presence of the streak. In addition to these features, in Fig. 3c we observe another set of superstructure reflections that are located at $(h \pm 2n\varepsilon, 0, l \pm n\varepsilon)$ with h and l being even, n an integer, and $\varepsilon \approx 2/7$. A sketch of this spot distribution is provided in Fig. 3d. Again, the first harmonics are

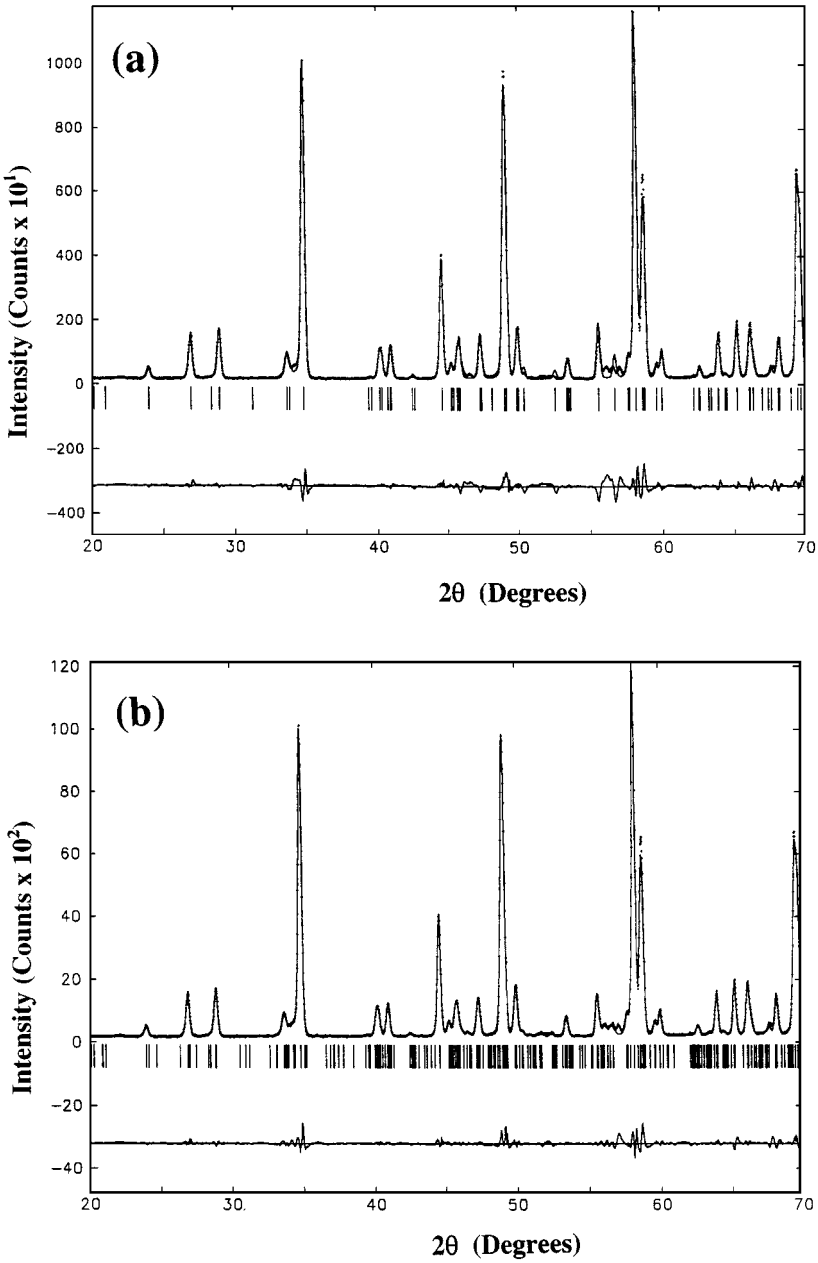

FIG. 2. Full-profile refinement plots of the high-resolution neutron powder diffraction data with (a) not taking into account any modulations and (b) including the modulations with $q_a = 0.2813(1)$ and $q_c = 0.1422(1)$.

significantly more intense than the higher harmonics. The dominance of the first harmonics in both cases suggests that the modulations are nearly sinusoidal.

We have made no attempt to determine the origin or detailed shape of the modulations giving rise to the satellite reflections described above nor have we established the nature of the disorder responsible for the streaking along **a*** and/or **c***. Presumably, these may be associated with long period in-plane distortions of the $\{Bi_2O_2\}^{2+}$ layers. Other superstructure patterns have been observed as well, indicating that there are many distortional modes present. Since our sampling is limited, we cannot comment on the frequency of observation of each of the superstructure patterns. Coherent intergrowths of two closely related symmetries ($Pca2_1$ with $C1a1$ in the standard setting) have been reported in TEM studies for both Bi_2MoO_6 and Bi_2WO_6 (23, 24), resulting in commensurate modulations along **b*** (in our standard setting). These additional commensurate

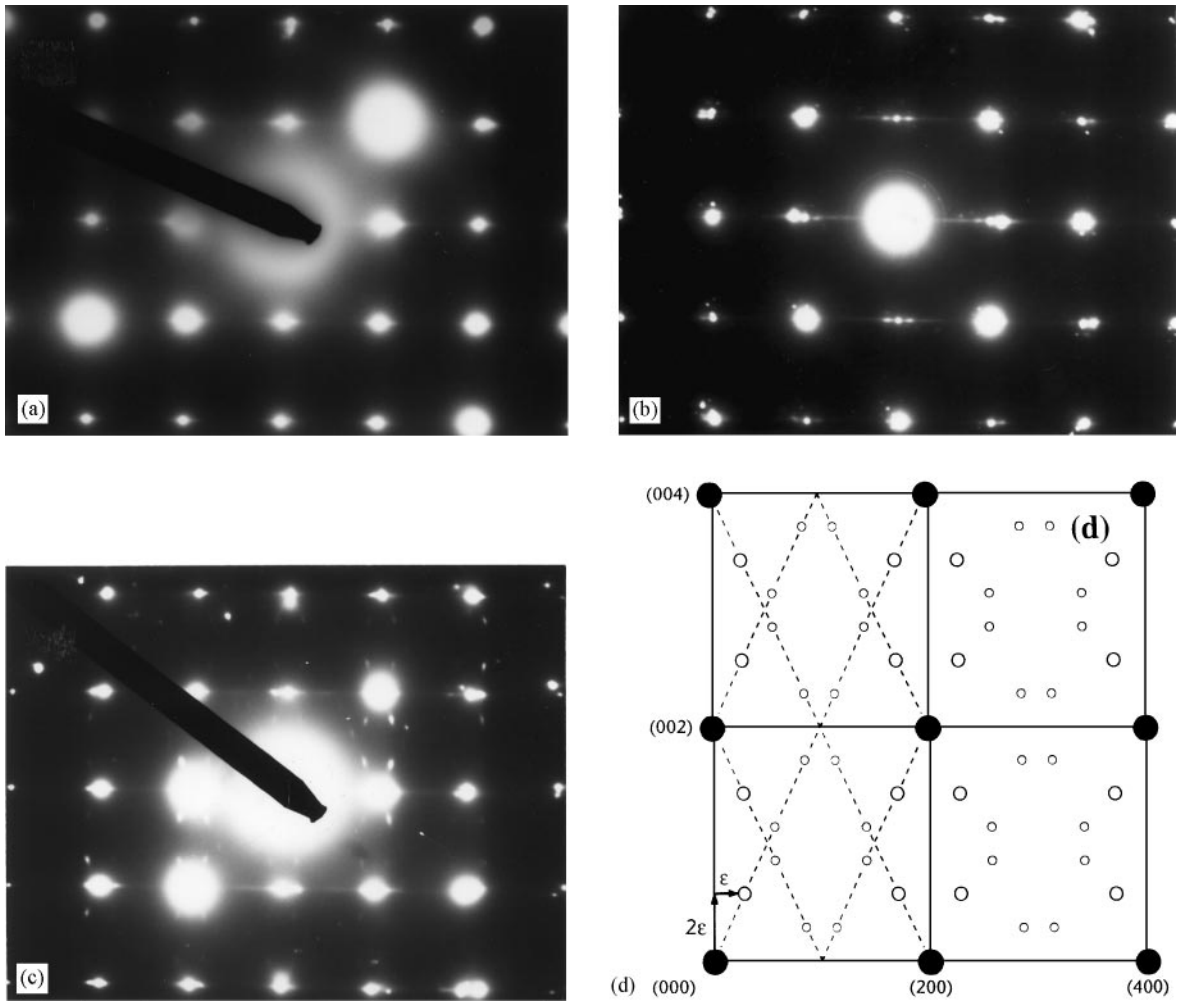

FIG. 3. Selected area electron diffraction patterns revealing (a) streaking along **a*** and/or **c***, (b) satellites occurring at $\sim(\pm n/4, 0, 0)$, and (c) satellites located at $(h \pm 2n\varepsilon, 0, l \pm n\varepsilon)$. A sketch of the spot distribution from (c) is presented in (d).

modulations should be distinguished from the in-plane incommensurations that we report. A detailed HREM study is required to unravel the true microscopic details of the incommensurate modulations in Bi_2MoO_6 and is beyond the scope of the present paper.

Full-profile refinements. Since the **a** and **c** axes are very similar, electron diffraction data do not allow the unambiguous assignment of the incommensurate wave vectors. Using a full-profile fitting routine in which the intensities are treated as variables, the high-resolution neutron powder diffraction data were refined against two different models. In model 1, $q_{\mathbf{a}} \approx 2/7$ and $q_{\mathbf{c}} \approx 4/7$, and in model 2, the reverse case of $\mathbf{q}_{\mathbf{a}} \approx 4/7$ and $q_{\mathbf{c}} \approx 2/7$. Model 2 fits the data better (Fig. 2b). To clarify this, high-resolution synchrotron data were taken and also revealed that model 2 fit the data better. A selected range from the synchrotron data set is shown in Fig. 3, indicating the well-resolved superstructure reflections. The synchrotron data gave $q_{\mathbf{a}} = 0.5626(2)$ and $q_{\mathbf{c}} = 0.2844(2)$. However, both data sets revealed that other peaks were present that could not be accounted for by this modulation. This is consistent with other modulations observed by selected area electron diffraction. We have thus far been unable to unambiguously locate the $q_{\mathbf{a}} \approx \frac{1}{4}$ superstructure reflections in either the X-ray or neutron powder data. This may in part be due to overlaps with the $(4/7, 0, 2/7)$ superstructure reflections.

Temperature-Dependent Studies

We collected data sets as 20, 300, 361, 570, 671, 777, 803, 819, 828, and 858 K, which were all refined using the Rietveld method. An extra data set at 470 K was taken with significantly lower counting statistics and only used to determine the lattice constants.

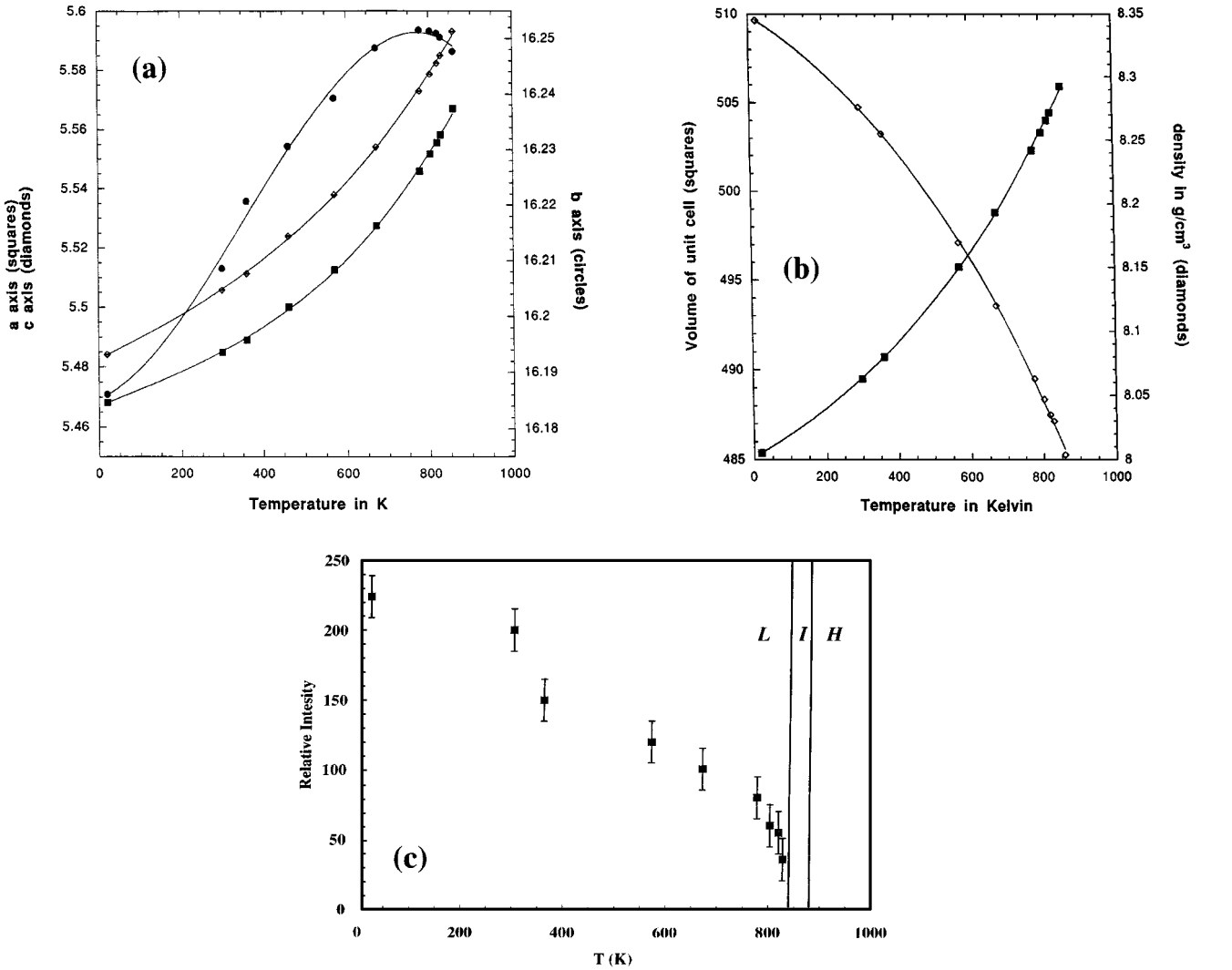

FIG. 4. Temperature dependence of (a) lattice constants, (b) cell volume and density, and (c) incommensurate superlattice intensity reflection assigned as (1.438, 0, 2.284).

Lattice expansion and the γ(L) to γ(I) transition. A highly anisotropic thermal response of unit cell parameters is observed upon heating (Fig. 4a). The pseudo-tetragonal **a** and **c** axes, along which the incommensurate modulations where found, expand almost identically. Even after the transition into the γ(I) phase, no discontinuity can be detected in **a** or **c**. On the other hand, the **b** axis expands rapidly with heating to 500 K, then starts to decrease, and contracts significantly on approach to the γ(I) phase. Since any charge transfer between the $\{Bi_2O_2\}^{2+}$ and $\{MoO_4\}^{2-}$ layers occurs along **b**, this thermal response is indicative of a change in the interlayer charge transfer. Despite this striking difference in intra- and interlayer thermal expansion, the unit cell volume, and thus the density, shows no discontinuity at the γ(L) to γ(I) transition (Fig. 4b). However, the intensities of the satellites attributed to incommensurate modulations decrease continuously with heating and are no longer observable in the γ(I) phase (Fig. 4c). Our last measured diffraction pattern at 858 K shows no indications of any these reflections and is 5 K above the transition temperature given by Erman and Gal'perin (24). We conclude that the γ(L) to γ(I) transition is a second-order incommensurate-to-commensurate phase transition. The reflection near $2\theta = 57.0^\circ$, which could not be accounted for with modulations with $q_a = 0.5626(2)$ and $q_c = 0.2844(2)$ in Fig. 2b, was found to remain above the γ(L)-to-γ(I) transition and remains of unknown origin.

Bond distances. The bond graph shown in Fig. 5 was prepared in such a way as to distinguish short, intermediate, and long bond distances for Bi–O and Mo–O using room temperature data. The criteria for these are somewhat

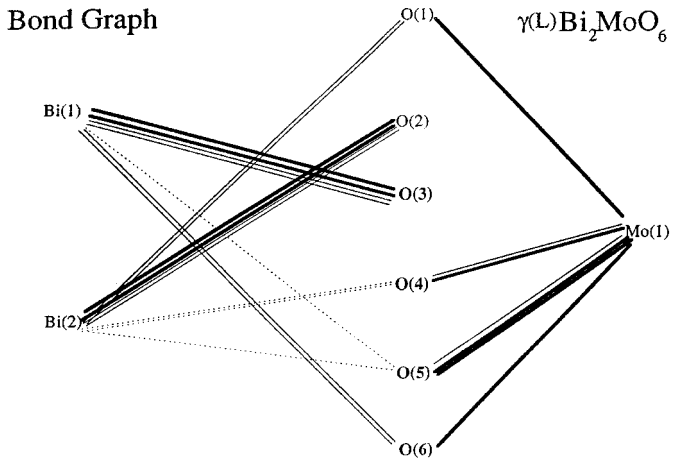

FIG. 5. Bond graph for γ(L)-Bi_2MoO_6. The outermost oxygens ([2] and [3]) are those located in Bi_2O_2 midplane. O[1] and O[6] are the "apical" oxygens, whereas O[4] and O[5] are the "basal" oxygens from the octahedral perspective. Note that the asymmetry of the diagram arises from the distribution of distant oxygens about the two bismuth sites.

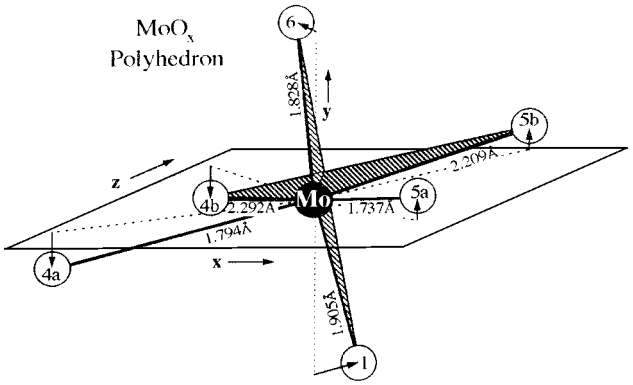

FIG. 6. Clinographic projection of the MoO_x coordination environment.

arbitrary, but match those used in our earlier paper on γ(H)-Bi_2MoO_6 (10). The short bonds are considered as those for which the valence sum $v_{ij} > 0.65$ and are represented by heavy solid lines. Long bonds are identified as those with $0.025 < v_{ij} < 0.16$ and represented by dashed lines. Intermediate bond lengths are shown by a fine solid line and any separations for which $v_{ij} < 0.025$ are not shown. For reference, $v_{ij} = 0.65$ corresponds to $d = 2.253$ Å for Bi–O and to $d = 2.066$ Å for Mo–O.

It seems that the coordination of the Mo site has characteristics of both octahedral and tetrahedral coordination, depending on the way in which it is viewed. The bond graph analysis clearly shows that the Mo polyhedron consists of four short Mo–O bonds plus two much more distant Mo–O bonds. Using coordinates for $T = 300$ K, a clinographic projection of the coordination environment about Mo is presented in Fig. 6. The relative bond lengths are difficult to appreciate in any orientation, so we have labeled the distances along each of the bonds. The "apical" oxygens, O[1] and O[6], are among the four short bonds (1.7–1.9 Å) and form an angle with molybdenum of about 150°, i.e., significantly larger than the ideal tetrahedral angle. The two long bonds (2.2–2.3 Å) lie in a plane that essentially bisects the 150° angle as shown. From the tetrahedral perspective, the steric influence of these more distant oxygens forces the anomalously large angle and compresses the remaining angles involving the short bonds. This same steric effect results in bond lengths that are somewhat larger for the "apical" sites than for the "basal short bonds". From the distorted octahedral perspective, the basal oxygens are nearly coplanar, but slightly canted out of the plane as indicated by the vertical arrows in Fig. 6.

The four short bonds have distances that are quite comparable to those of the tetrahedra in the high-temperature γ(H) polymorph. Note in Table 1 that the four short Mo–O distances about each Mo site in γ(H) are listed using the site labels from Ref. (1) and that these also fall in the range 1.7–1.9 Å.

We next consider the temperature dependence of the Mo–O distances and angles in γ(L) and γ(I). van den Elzen *et al.* (26) collected X-ray diffraction data for γ-Bi_2MoO_6 from room temperature up to high temperature to examine the structural evolution and phase transitions. They suggested that the γ(L) to γ(I) transition may involve a change from octahedral to tetrahedral coordination such that the γ(I) structure may resemble La_2MoO_6. Based on EXAFS data, Sankar *et al.* (27) recently reported a change from γ(L) to γ(I) involving a progressive increase in the octahedral distortion with heating such that the octahedra are on the verge of becoming tetrahedra. In agreement with them, the results of our refinements indicate that although there are changes in

TABLE 1
Listing of Mo–O Bond Lengths for γ(H) from Ref. (1) for Comparison with Those for γ(L)

Mo[1]–O[19]	1.718(12)	Mo[2]–O[10]	1.751(12)	Mo[3]–O[22]	1.777(12)	Mo[4]–O[23]a	1.747(12)
Mo[1]–O[1]	1.719(12)	Mo[2]–O[6]	1.764(12)	Mo[3]–O[13]	1.781(12)	Mo[4]–O[15]a	1.771(12)
Mo[1]–O[2]a	1.765(12)	Mo[2]–O[9]a	1.819(12)	Mo[3]–O[12]	1.823(12)	Mo[4]–O[16]	1.787(12)
Mo[1]–O[17]	1.854(12)	Mo[2]–O[7]	1.835(12)	Mo[3]–O[14]	1.871(12)	Mo[4]–O[24]	1.814(12)

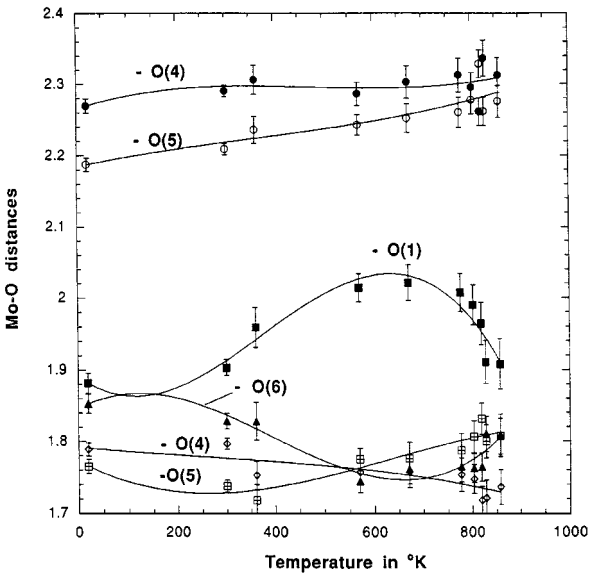

FIG. 7. The variation of the Mo–O distances in γ(L)-Bi_2MoO_6 as a function of temperature.

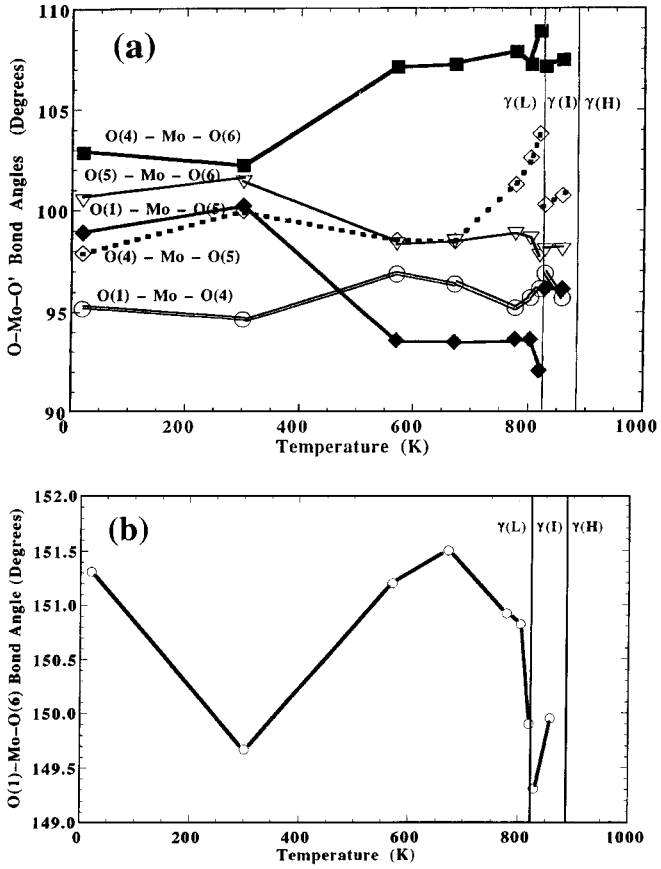

FIG. 8. Molybdenum–oxygen bond angles for (a) those in the range $100^\circ \pm 10^\circ$ and (b) the anomalously large O[1]–Mo–O[6] case.

the MoO_x polyhedra with temperature and that there are clear indications of the $\gamma(L) \rightarrow \gamma(I)$ transition, there is no simple change of coordination here. The thermal evolution of the oxygen bond distances is presented in Fig. 7. Note that the maximum difference between the two apical Mo–O distances occurs in the range 600–800 K. Afterward, these two distances rapidly converge upon approach to the $\gamma(L)/\gamma(I)$ phase transition, above which there is little further change. Nothing unusual is observed in the variation of the equatorial Mo–O bond distances, except very near the phase transition. Table 2 contains a listing of individual bond lengths at each temperature.

The thermal evolution of bond angles is presented in Fig. 8. Once again, note that one large angle results from the steric effect of the two more distant ("intermediate length") Mo–O bonds and the remaining angles associated with the shorter bonds, as a consequence, compressed. Note also that these intermediate length bonds involve O[4] and O[5] and are thus in the basal plane. They result from the acentric positioning of the molybdenum in the $\{MoO_4\}$ basal network. For comparison, the O–Mo–O tetrahedral angles in γ(H) range from 102° to 125° and each Mo site has one rather large angle ($> 118^\circ$), not unlike γ(L) but less extreme.

Next, we consider the distinguishable $\{Bi_2O_2\}^{2+}$ layers in terms of the bond graph analysis. In both $\{Bi_2O_2\}^{2+}$ layers there are two short and two intermediate length bonds to the midline oxygens (i.e., O[3] for Bi[1] and O[2] for Bi[2]). Each Bi site also has two intermediate length bonds to the "apical" oxygens (i.e., O[6] for Bi[1] and O[1] for Bi[2]). As

TABLE 2
Temperature Dependence of Mo–O Bond Lengths

	20 K	300 K	570 K	671 K	777 K	803 K	819 K	828 K	858 K
Mo–O[1]	1.8802	1.9047	2.0140	2.0138	2.0060	1.9954	1.9685	1.9021	1.9101
Mo–O[4]	1.7857	1.7942	1.7593	1.7538	1.7525	1.7501	1.7206	1.7199	1.7357
	2.2707	2.2924	2.2876	2.3044	2.3129	2.2955	2.2628	2.3362	2.3129
Mo–O[5]	1.7650	1.7375	1.7706	1.7746	1.7908	1.8051	1.8293	1.7982	1.8046
	2.1892	2.2091	2.2435	2.2550	2.2572	2.2749	2.3280	2.2634	2.2749
Mo–O[6]	1.8520	1.8278	1.7451	1.7613	1.7632	1.7628	1.7574	1.8151	1.8084

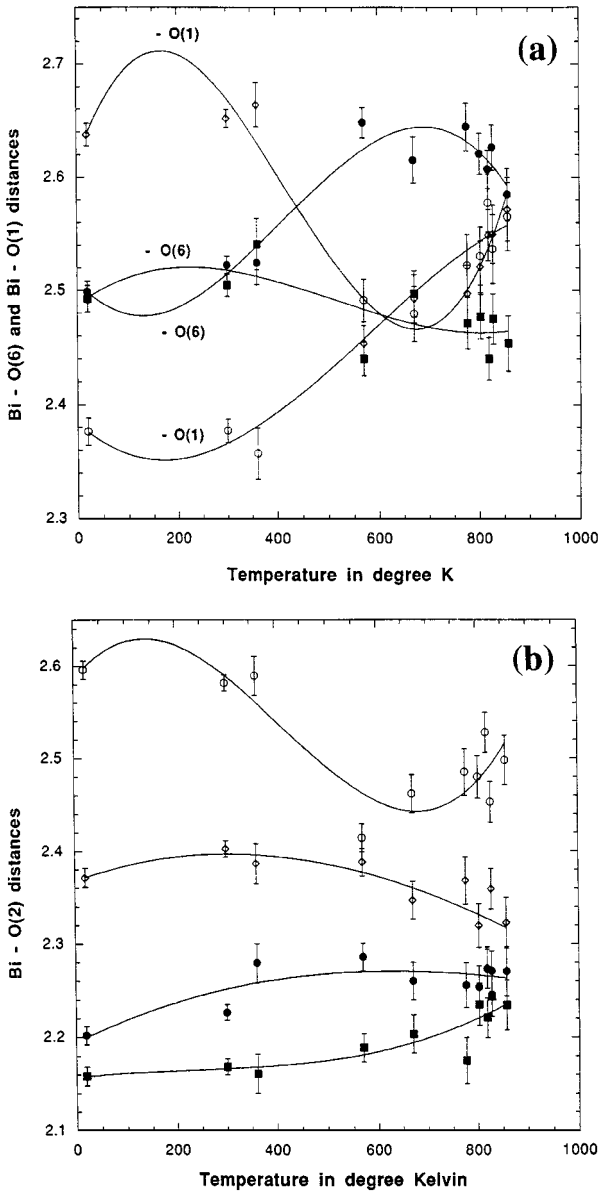

FIG. 9. Temperature dependence of the Bi–O distances for (a) interlayer O[1] and O[6] and (b) for intralayer O[2].

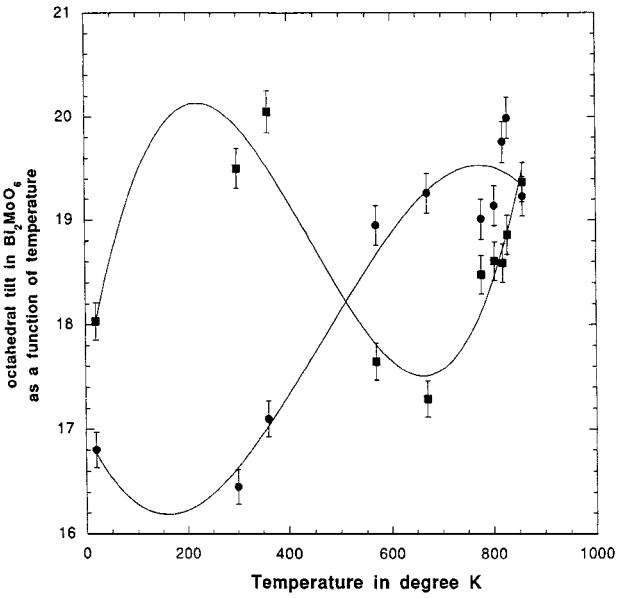

FIG. 10. The octahedral tilts (in degrees): α around **b** and β around **a** as a function of temperature.

expected, the distances to the basal oxygens O[4] and O[5] are rather large. The distinction between these layers is fairly subtle and is primarily identifiable by the smaller short distances for Bi[2]–O[2] relative to Bi[1]–O[3]. As we will point out later, the valence sums are similar for these oxygens, but the site potentials are quite distinct.

The changes in the bismuth coordination with temperature are twofold: The distances to the apical O[1] and O[6] atoms at low temperatures reveal two very close Bi[1]–O[6] distances and two very different Bi[2]–O[1] distances (Fig. 9a). As the distance dispersion of the oxygens with respect to molybdenum occurs (i.e., Mo–O[6] contracts, Mo–O[1] expands), the two Bi[1]–O[6] distances expand and grow apart, whereas the two Bi[2]–O[1] distances contract and come together.

The thermal response of the oxygens within the $\{Bi_2O_2\}^{2+}$ layers reveal the strongest variation *in the longest* Bi[2]–O[2] and Bi[1]–O[3] distances (see Fig. 9b).

TABLE 3
Temperature Dependence of O–Mo–O Bond Angles

	20 K	300 K	570 K	671 K	777 K	803 K	819 K	828 K	858 K
O[1]–Mo–O[4]	95.17°	94.64°	96.86°	96.38°	95.21°	95.70°	96.15°	96.88°	95.69°
O[1]–Mo–O[5]	98.90°	100.22°	93.58°	93.50°	93.64°	93.64°	92.07°	96.17°	96.15°
O[1]–Mo–O[6]	1151.31°	149.67°	151.20°	151.50°	150.92°	150.82°	149.90°	149.31°	149.95°
O[4]–Mo–O[5]	97.89°	99.97°	98.51°	98.47°	101.27°	102.60°	103.81°	100.27°	100.72°
O[4]–Mo–O[6]	102.86°	102.24°	107.10°	107.22°	107.85°	107.22°	108.87°	107.12°	107.44°
O[5]–Mo–O[6]	100.49°	101.41°	98.32°	98.46°	98.80°	98.58°	97.73°	98.01°	98.02°
average:	107.77°	107.87°	107.60°	107.59°	107.95°	108.09°	108.09°	107.96°	108.00°

Being twice subjected to a *trans* effect induced via O[1] or O[6], these are the weakest and thus the longest Bi–O distances. Any variation in the interlayer charge transfer via O[1] and O[6] will most strongly effect this bond distance.

Octahedral tilts. In Bi_2MoO_6, the MoO_6 octahedra are rotated by an angle θ relative to the ideal basal MoO_6 network around the unique axis **b** and by an angle of ϕ around **a**. The tilting around **a** brings the two apical oxygens O[1] and O[6] closer to the Bi atoms. The refined structural parameters reveal that these two octahedral tilts behave differently when the structure is heated (Fig. 10). The initial increase in θ upon heating to 400 K is accompanied by expansion of the lattice constants. Above 400 K, the two apical Mo–O distances involving O[1] and O[6] grow apart, leading to a charge separation. It appears that the θ tilt is therefore influenced by the interlayer charge separation. The ϕ tilt around **a** increases up to 600 K and then levels off between 600 and 800 K. This coincides with the loss of the incommensurations in the **ac** plane. ϕ is responding to changes in the mismatch of distances between the $\{MoO_4\}^{2-}$ and $\{Bi_2O_2\}^{2+}$ layers and is indirectly related to changes in charge transfer.

CONCLUSION

We have identified the distinction between the γ(L) and γ(I) forms as being primarily due to the presence or absence, respectively, of incommensurate in-plane modulations. Upon heating, this incommensurate modulation gradually disappears, leading to the second-order incommensurate/commensurate transition. This transition occurs about 40 K below the first-order irreversible (strongly reconstructive) transition into the fluorite-related high-temperature modification, γ(H). The thermal evolution of the incommensurate γ(L) phase may be related to changes in the interlayer charge transfer between two different $\{Bi_2O_2\}^{2+}$ layers and their adjacent $\{MoO_4\}^{2-}$ layers. This interlayer charge transfer may also be a contributing factor in the performance of this material for selective oxidation and ammoxidation of olefins.

ACKNOWLEDGMENTS

The authors wish to gratefully acknowledge R. K. Grasselli for helpful discussions. Support for this work was provided by the DuPont Co. and from the Division of Materials Sciences, U.S. Department of Energy under (BNL) Contract DE-AC02-76CH00016.

REFERENCES

1. R. K. Grasselli and J. D. Burrington, *Adv. Catal.* **30,** 133 (1981); Y. Moro-Oka and W. Ueda, *Adv. Catal.* **40,** 233 (1994); R. K. Grasselli, *J. Chem. Educ.* **63,** 216 (1986).
2. J. L. Callahan and R. K. Grasselli, *AIChE J.* **9,** 755 (1963).
3. A. F. van den Elzen and G. D. Rieck, *Acta Crystallogr. Sect. B* **29,** 2436 (1973); F. Theobald, A. Laarif, and A. W. Hewat, *Mater. Res. Bull.* **20,** 653 (1985).
4. A. F. van de Elzen and G. D. Rieck, *Mater. Res. Bull.* **10,** 1163 (1975); H. Y. Chen and A. W. Sleight, *J. Solid State Chem.* **63,** 70 (1986).
5. D. J. Buttrey, D. A. Jefferson, and J. M. Thomas, *Philos. Mag. A* **53,** 897 (1986).
6. B. Aurivillius, *Ark. Kemi* **2,** 519 (1949).
7. A. F. van den Elzen and G. D. Rieck, *Acta Crystallogr. Sect. B* **29,** 2436 (1973); R. G. Teller, J. F. Brazdil, R. K. Grasselli, and J. D. Jorgensen, *Acta Crystallogr. Sect. C* **40,** 2001 (1984).
8. G. Blasse, *J. Inorg. Nucl. Chem.* **28,** 1124 (1966); P. L. Gai, *J. Solid State Chem.* **49,** 25 (1983).
9. H. Kodama and A. Watanabe, *J. Solid State Chem.* **56,** 225 (1985).
10. D. J. Buttrey, T. Vogt, U. Wildgruber, and W. R. Robinson, *J. Solid State Chem.* **111,** 118–127 (1994).
11. R. N. Vannire, G. Mairesse, F. Abraham, and G. Nowogrocki, *J. Solid State Chem.* **122,** 394–406 (1996).
12. D. J. Buttrey, T. Vogt, G. Yap, and A. L. Rheingold, *Mater. Res. Bull.* **32,** 947 (1997).
13. D. J. Buttrey, D. A. Jefferson, and J. M. Thomas, *Mater. Res. Bull.* **21,** 739 (1986).
14. M. Kunz and I. D. Brown, *J. Solid State Chem.* **115,** 395 (1995).
15. S. Seong, K. Yee, and T. A. Albright, *J. Am. Chem. Soc.* **115,** 1981 (1993).
16. C. Torrardi, private communication.
17. F. Theobald, A. Laarif, and A. W. Hewat, *Ferroelectrics* **56,** 219–237 (1984).
18. T. Vogt, L. Passell, S. Cheung, and J. D. Axe, *NIM A* **338,** 71 (1994).
19. J. D. Axe, S. Cheung, D. E. Cox, L. Passell, T. Vogt, and S. Bar-Ziv, *J. Neutron Res.* **2**(3), 85 (1994).
20. H. M. Rietveld, *J. Appl. Crystallogr.* **2,** 65 (1969).
21. J. K. Cockcroft and A. N. Fitch, *Z. Kristallogr.* **184,** 123 (1988).
22. I. H. Ismailzade, I. M. Aliyev, R. M. Ismailov, A. I. Alekberov, and D. A. Rzayev, *Ferroelectrics* **22,** 853–854 (1979).
23. A. D. Rae, J. G. Thompson, and R. L. Withers, *Acta Crystallogr. B* **47,** 870 (1991).
24. J. G. Thompson, S. Schmid, R. L. Withers, A. D. Rae, and J. D. Fitzgerald, *J. Solid State Chem.* **101,** 309 (1991).
25. L. Y. Erman and E. L. Gal'perin, *Russ. J. Inorg. Chem.* (Engl. Transl.) **13,** 487 (1968).
26. A. F. van den Elzen, L. Boon, and R. Metselaar, "Solid State Chemistry." Elsevier, Amsterdam, 1982.
27. G. Sankar, M. A. Roberts, J. M. Thomas, G. U. Kulkarni, N. Rangavittal, and C. N. R. Rao, *J. Solid State Chem.* **119,** 210 (1995).
28. I. D. Brown and D. Altermatt, *Acta Crystallogr. Sect. C* **41,** 244 (1985).